Materials Horizons

ROYAL SOCIETY OF CHEMISTRY

COMMUNICATION

View Article Online
View Journal

Cite this: DOI: 10.1039/d5mh01250c

Received 30th June 2025,
Accepted 23rd July 2025

DOI: 10.1039/d5mh01250c

rsc.li/materials-horizons

Hyperelastic superomniphobic surfaces *via* microprotrusion-induced stress redistribution†

Mohammad Javad Zarei, Sreekiran Pillai, Omar Eldaly, Adil Majeed Rather, Sravanthi Vallabhuneni, Mohammed A. Zikry and Arun Kumar Kota *

In this work, we report hyperelastic superomniphobic surfaces that have been engineered to retain superomniphobicity, without coating delamination, even at 400% strain and after thousands of stretch–release cycles. To achieve such hyperelastic superomniphobic surfaces, we introduce a novel design – an array of discrete microprotrusions on the hyperelastic material that redistribute the stresses out-of-plane during elongation. Such an out-of-plane redistribution of stresses results in nearly stress-free tops of the microprotrusions, allowing the coating to be virtually intact even after 5000 stretch–release cycles. Furthermore, through systematic experiments and theoretical analysis, we studied the influence of elongation on contact angles, sliding angles and breakthrough pressures on our hyperelastic superomniphobic surfaces. We envision that our robust hyperelastic superomniphobic surfaces will have a wide range of applications in wearable electronics, textiles, artificial skins, droplet manipulation and protective wraps.

New concepts

We present a novel approach for designing hyperelastic superomniphobic surfaces that maintain their extreme liquid repellency even under 400% strain and after thousands of stretch release cycles. Our strategy leverages an innovative array of discrete microprotrusions on the hyperelastic substrate, which redistributes mechanical stresses out-of-plane during elongation. This unique stress distribution strategy minimizes strain at the microprotrusion tops, thereby preserving the integrity of the superomniphobic coatings even after 5000 deformation cycles. Through systematic experiments and theoretical modelling, we analyse the effects of stretching on wettability through contact angles, sliding angles and breakthrough pressures. Our findings establish a new paradigm for mechanically resilient superomniphobic surfaces, with promising applications in wearable electronics, textile, artificial skins, droplet manipulation and protective coatings.

1. Introduction

Super-repellent surfaces are extremely repellent to liquids.[1,2] In the last few years, there has been increasing interest in stretchable super-repellent surfaces because of their applications in textile,[3] biomedical[4,5] and wearable electronics fields.[6] Super-repellent surfaces can be broadly classified into superhydrophobic surfaces[7] (*i.e.*, surfaces that are extremely repellent to high surface tension liquids like water) and superomniphobic surfaces[8] (*i.e.*, surfaces that are extremely repellent to both high surface tension liquids like water and low surface tension liquids like oils). While superhydrophobic surfaces can be easily fabricated with a wide range of textures, superomniphobic surfaces are more difficult to fabricate as they require reentrant textures.[9] As a result, most prior reports have focused on stretchable superhydrophobic surfaces, which are easier to fabricate.[10–12] For instance, Ju *et al.* reported a stretchable and robust superhydrophobic surface fabricated by combining physical encapsulation and chemical bonding on Ecoflex.[10] Hu *et al.* reported a highly stretchable and mechanically stable superhydrophobic surface fabricated by a facile spray coating of a carbon black/polybutadiene elastomeric composite on a rubber substrate followed by thermal curing.[11] Similarly, Wang *et al.* developed a stretchable superhydrophobic film by a two-step spray method and subsequent demolding.[12] In contrast, there are very few reports on stretchable superomniphobic surfaces.[13,14] For instance, Zhou *et al.* fabricated a stretchable superamphiphobic surface by spray-coating silicone nanofilaments onto a pre-stretched substrate followed by fluorination.[13] Tian *et al.* fabricated stretchable superomniphobic electrodes *via* the synergistic combination of *in situ* growth of silver nanoparticles (AgNPs)/acid-modified carbon nanotubes followed by fluorination.[14] However, all prior stretchable superomniphobic surfaces exhibit superomniphobicity at $<250\%$ strain. In this work, we report the first ever hyperelastic superomniphobic surfaces that have been engineered to retain superomniphobicity at strains as high as 400% and after thousands of stretch release cycles. Our hyperelastic superomniphobic surfaces consist of hyperelastic

Department of Mechanical and Aerospace Engineering, North Carolina State University, Raleigh, NC 27695, USA. E-mail: akota2@ncsu.edu

† Electronic supplementary information (ESI) available. See DOI: https://doi.org/10.1039/d5mh01250c

materials (*i.e.*, materials which display large elastic deformations) spray coated with a superomniphobic coating. To prevent delamination of the superomniphobic coating at very high strains, we introduce a novel design – an array of discrete microprotrusions on the hyperelastic material that redistribute the stresses during elongation. Such redistribution of stresses allows the retention of superomniphobicity even after 5000+ stretch–release cycles. Furthermore, through systematic experiments and theoretical analysis, we studied the influence of elongation on contact angles, breakthrough pressures and sliding angles on our hyperelastic superomniphobic surfaces. We envision that our robust hyperelastic superomniphobic surfaces will have a wide range of applications in wearable electronics, textiles, artificial skins, droplet manipulation and protective wraps.

In order to fabricate hyperelastic superomniphobic surfaces, it is essential to have a good understanding of the fundamentals of wetting that lead to superomniphobicity.[15] The primary measure of wetting of a liquid on a nontextured (*i.e.*, smooth) solid surface is the Young's contact angle θ.[16] Typically, surfaces with low solid surface energy γ_{sv} result in high Young's contact angles.[17–19] To design super-repellent surfaces, in addition to low solid surface energy, a surface texture (or roughness) is necessary.[20,21] When a liquid droplet comes into contact with a textured solid surface, it displays an apparent contact angle θ^*, which is different from the Young's contact angle θ. On the textured solid surface, the droplet can assume either the Wenzel state[22] or the Cassie–Baxter state.[23] In the Wenzel state, the liquid droplet completely penetrates the surface texture, while in the Cassie–Baxter state, there are pockets of air trapped within the surface texture beneath the droplet. The reduced solid–liquid contact area and the increased liquid–air contact area in the Cassie–Baxter state often allow droplets to display very high apparent advancing and receding contact angles, θ^*_{adv} and θ^*_{rec}, as well as very low contact angle hysteresis $\Delta\theta^* = \theta^*_{adv} - \theta^*_{rec}$.[24–27] Such low contact angle hysteresis results in high mobility of the droplets with very low sliding angle ω (the minimum angle by which the surface must be tilted relative to the horizontal for the droplet to slide).[28,29] As a result, the Cassie–Baxter state is preferred for designing super-repellent surfaces with apparent contact angles $\theta^* > 150^\circ$ and sliding angles $\omega < 10^\circ$. Surfaces are considered superhydrophobic if they exhibit $\theta^* > 150^\circ$ and $\omega < 10^\circ$ for high surface tension liquids (*e.g.*, water)[7] and superomniphobic if they exhibit $\theta^* > 150^\circ$ and $\omega < 10^\circ$ for high surface tension liquids as well as low surface tension liquids (*e.g.*, oils).[30,31] Unlike superhydrophobic surfaces, re-entrant texture (*e.g.*, convex, overhang or undercut texture) is necessary to design superomniphobic surfaces.[19] Many prior reports have demonstrated superomniphobicity through an appropriate combination of re-entrant texture and low solid surface energy.[8,18,30–35]

2. Results and discussion

Building on this understanding, a hyperelastic material can be rendered superomniphobic by imparting re-entrant texture and low solid surface energy to its surface. A simple, economical and scalable way of rendering a surface superomniphobic is by spray coating it with fluorinated silica particles.[8,35,36] When a hyperelastic material is coated with such fluorinated silica particles, the combination of re-entrant texture offered by silica particles and low solid surface energy offered by fluorination render the surface superomniphobic (Fig. 1a). However, when the hyperelastic material spray coated with fluorinated silica particles experiences high strains, the coating delaminates due to high stresses at the coating–hyperelastic material interface (Fig. 1b), resulting in loss of superomniphobicity. To retain superomniphobicity at very high strains (that are typical for hyperelastic materials), it is essential to prevent or reduce delamination of the coating from the hyperelastic material. Here, we introduce a novel way to overcome this delamination by introducing an array of microprotrusions that can redistribute the stresses out-of-plane. Consider a monolithic hyperelastic material with an array of microprotrusions that have been coated with particles (Fig. 1c). When such a spray coated hyperelastic material with an array of microprotrusions experiences high strains, the high stresses are primarily concentrated between the microprotrusions, leaving the top of the microprotrusions nearly stress-free (Fig. 1d). Such microprotrusion-induced out-of-plane redistribution of stresses on a hyperelastic material compared to a hyperelastic material without microprotrusions is evident from numerical simulations (see Fig. 1g–j, Fig. S1, Movie S1, Supplementary Information 1 and the Experimental section, ESI†). In the stretched state, while the hyperelastic material without microprotrusions displays relatively uniform normal stresses σ_{xx} along the surface (shown in green in Fig. 1h), the hyperelastic material with microprotrusions displays higher normal stresses σ_{xx} between the microprotrusions (shown in red in Fig. 1j) and negligible σ_{xx} at the top surface of the microprotrusions (shown in gray in Fig. 1j). While high stresses lead to delamination of the coating between the microprotrusions, the negligible stresses at the top surface of the microprotrusions allow the coating to be virtually intact even after multiple stretch-release cycles (Fig. 1e and f). On such a hyperelastic material with an array of microprotrusions, although there is delamination of the coating between the microprotrusions, the virtually intact coating on the top allows the surface to retain its superomniphobicity, both at unstretched and stretched states (in this sense, superomniphobicity is a tolerant material property). Here, it must be noted that the primary function of the microprotrusions is to redistribute the normal stresses (due to extensive curvature; see Movie S1, Fig. S1 and Section S1, ESI†) to prevent or reduce delamination, rather than creating a hierarchical structure (*i.e.*, a finer texture superimposed on a coarser texture) to enhance superomniphobicity.

In this work, we fabricated hyperelastic superomniphobic surfaces using a siloxane elastomer (Ecoflex 00-50) as a substrate (Fig. 2; see the Experimental section). We chose the siloxane elastomer because it is a hyperelastic material with very high stretchability (strain to failure $\approx$560%; see Section S2, Fig. S2 and the Experimental section, ESI†). We fabricated the siloxane elastomer with microprotrusions *via* micromolding, using a stainless steel wire mesh (wire diameter $\approx$55 μm and

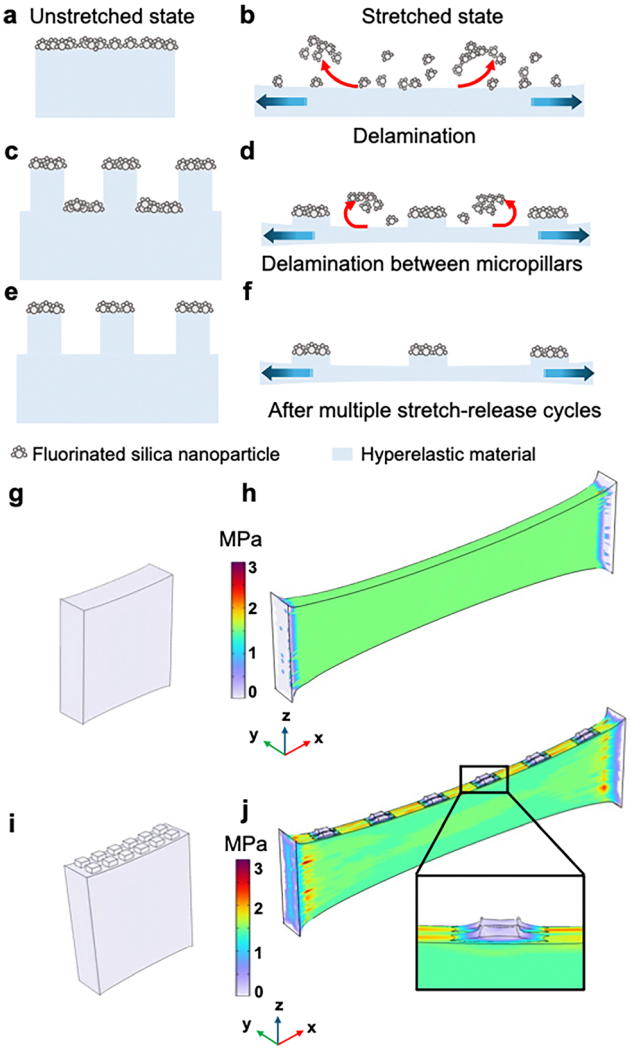

Fig. 1 Microprotrusion-induced stress redistribution. (a) Schematic depicting a hyperelastic material coated with fluorinated silica particles, at the unstretched state. (b) Schematic depicting coating delamination due to high stresses at the coating–hyperelastic material interface, at the stretched state. (c) Schematic depicting a monolithic hyperelastic material with an array of microprotrusions coated with fluorinated silica nanoparticles, at the unstretched state. (d) Schematic depicting coating delamination between the microprotrusions, but virtually intact coating on the nearly stress-free tops of the microprotrusions, at the stretched state. (e) and (f) Schematics depicting that the stress-free tops of the microprotrusions allow the coating to be virtually intact even after multiple stretch-release cycles. (g) and (h) Numerical simulations depicting the normal stress σ_{xx} distribution on the hyperelastic material without microprotrusions at the unstretched and stretched states, respectively. (i) and (j) Numerical simulations depicting the normal stress σ_{xx} distribution on the hyperelastic material with microprotrusions at the unstretched and stretched states, respectively. The inset in (j) depicts negligible σ_{xx} at the top surfaces of the microprotrusions. Colors represent the magnitude of stress in (g)–(j).

opening size ≈75 μm) as the mold. Then, we coated the substrates with a polyurethane-based adhesive (VytaFlex 10), followed by coating with fluorinated silica particles (see the Experimental section). We used the adhesive layer to ensure good adhesion between the siloxane elastomer and the fluorinated silica particles. We chose fluorinated silica particles because (i) the surface of silica particles can be easily modified with fluoroalkyl silanes to achieve low solid surface energy ($\gamma_{sv} \approx 12$ mN m^{-1}; see Section S3, ESI†) and (ii) microscale agglomerates of the nanoscale silica particles offer re-entrant texture. The combination of low solid surface energy and re-entrant texture of the fluorinated silica particle layer would result in superomniphobicity. Upon stretching and releasing such hyperelastic superomniphobic surfaces, we posited that the fluorinated silica particles between the microprotrusions would delaminate due to the high interfacial stresses, but the fluorinated silica particles on top of the microprotrusions would remain virtually intact due to the low interfacial stresses.

To better understand the hyperelastic superomniphobic surfaces, let us first consider the unstretched state. Prior to coating with the polyurethane-based adhesive and the fluorinated silica particles, the morphology of the micromolded siloxane elastomer showed ∼80 μm × 80 μm microprotrusions with a spacing of ∼50 μm (Fig. 3a; see the Experimental section), indicating a reasonably faithful reproduction of the stainless steel wire mesh mold. Then, the substrate was coated with polyurethane-based adhesives and fluorinated silica particles. The surface morphology (Fig. 3b) of the unstretched substrate consisted of microscale agglomerates (∼50–100 μm) of fluorinated silica particles with a re-entrant texture. Fourier transform infrared spectroscopy (FTIR) of the fluorinated silica particles (Fig. 3c; see the Experimental section) confirmed the presence of fluorocarbon functional groups (which impart low solid surface energy γ_{sv}) at the surface, with strong absorption peaks around 1200 cm^{-1} corresponding to the –CF_2 and –CF_3 group stretching, as well as absorption peaks around 575 cm^{-1}, 730 cm^{-1} and 1120 cm^{-1} corresponding to the vibration of the C–F bond of –CF_2 and –CF_3 groups.[37,38] The combination of re-entrant texture and low solid surface energy resulted in superomniphobicity in the unstretched state, with high apparent contact angles and low sliding angles for a wide range of liquids (Fig. 3d) from water (surface tension, γ_{lv} = 72.1 mN m^{-1}; a representative high surface tension liquid) to hexadecane (γ_{lv} = 27.5 mN m^{-1}; a representative low surface tension liquid). Water displayed $\theta^*_{adv} \approx 162^\circ$, $\theta^*_{rec} \approx 159^\circ$ and $\omega \approx 3^\circ$, and hexadecane displayed $\theta^*_{adv} \approx 154^\circ$, $\theta^*_{rec} \approx 149^\circ$ and $\omega \approx 6^\circ$ for 10 μL droplets. Superomniphobicity is also evident from liquid droplets beading up (Fig. 3e) and sliding easily (Movie S2, ESI†) on the surface in the unstretched state.

Now, let us consider the stretched state for siloxane elastomers without and with microprotrusions, coated with polyurethane-based adhesive and fluorinated silica particles. For coated siloxane elastomers without microprotrusions, up to strain <100%, the surfaces were superomniphobic (*e.g.*, $\theta^*_{adv} \approx 159^\circ$, $\theta^*_{rec} \approx 155^\circ$ and $\omega \approx 5^\circ$ for 10 μL water droplets and $\theta^*_{adv} \approx 155^\circ$, $\theta^*_{rec} \approx 148^\circ$ and $\omega \approx 8^\circ$ for 10 μL hexadecane droplets at 100% strain; see Section S4 and Fig. S3, ESI†). However, at strain >200%, the surfaces lost their superomniphobicity (*e.g.*, $\theta^*_{adv} \approx 145^\circ$, $\theta^*_{rec} \approx 137^\circ$ and $\omega \approx 19^\circ$ for 10 μL water droplets and $\theta^*_{adv} \approx 134^\circ$ and $\theta^*_{rec} \approx 121^\circ$ with no sliding

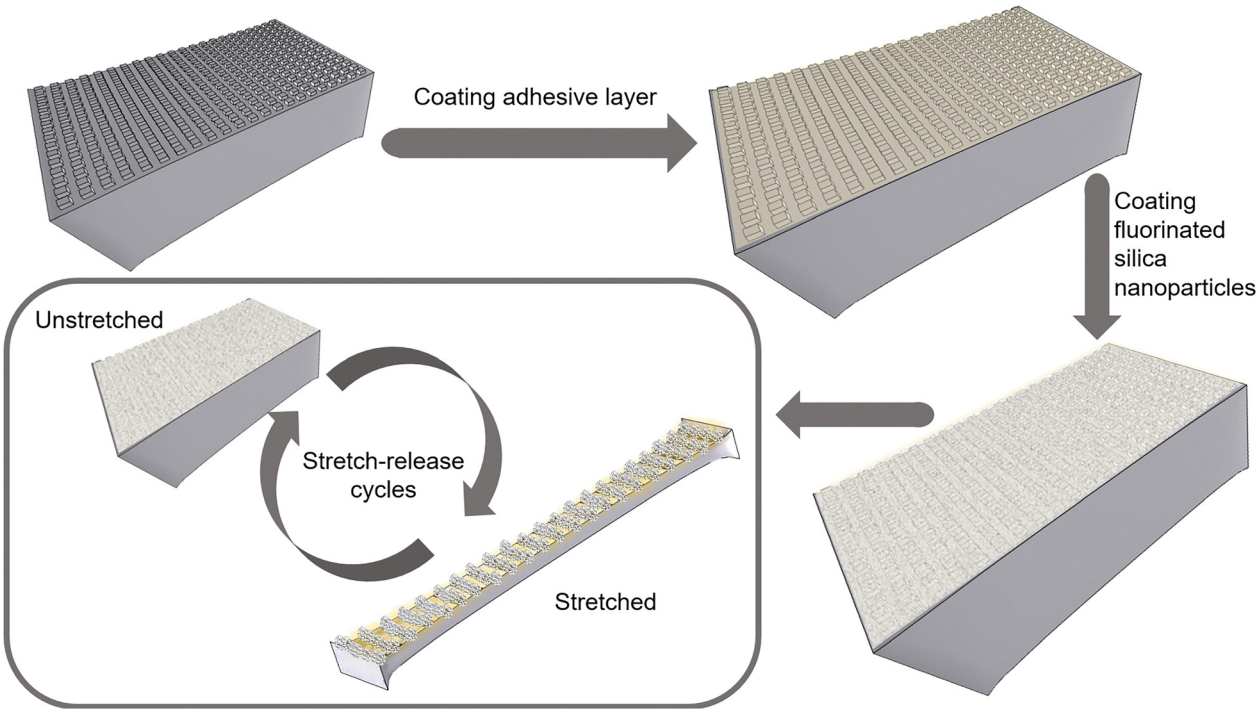

Fig. 2 Fabrication of the hyperelastic superomniphobic surface. Schematic depicting the fabrication steps and structure during stretch-release cycles.

for 10 μL hexadecane droplets at 300% strain) because the coating delaminated due to high stresses at the coating–hyperelastic material interface. In contrast, for coated siloxane elastomers with microprotrusions, the surfaces were superomniphobic up to 400% strain (*e.g.*, water displayed $\theta^*_{adv} \approx 162^\circ$, $\theta^*_{rec} \approx 159^\circ$ and $\omega \approx 2^\circ$, and hexadecane displayed $\theta^*_{adv} \approx 156^\circ$, $\theta^*_{rec} \approx 152^\circ$ and $\omega \approx 5^\circ$ for 10 μL droplets at 400% strain; Fig. 4a and Movie S3, ESI†). Furthermore, at different strains (from 100 to 400%), our hyperelastic surface displayed high apparent contact angles and sliding angles for a wide range of liquids (Fig. 4b and d) from water (surface tension, γ_{lv} = 72.1 mN m^{-1}; a representative high surface tension liquid) to hexadecane (γ_{lv} = 27.5 mN m^{-1}; a representative low surface tension liquid). This indicates that the out-of-plane redistribution of stress prevents delamination of the coating from the nearly stress-free tops of the microprotrusions, although there is delamination of the coating between the microprotrusions. An inspection of the surface morphology in the stretched state indeed confirms that the fluorinated silica particles are mostly intact on tops of the microprotrusions and minimal between the microprotrusions (Fig. 4c).

Our hyperelastic superomniphobic surfaces retain their superomniphobicity even after undergoing a diverse range of deformations. First, we investigated the retention of superomniphobicity of our surfaces upon exposure to liquids with a wide range of pH values. Our contact angle and sliding angle measurements for hexadecane indicated that the hyperelastic superomniphobic surfaces retained their superomniphobicity at the stretched state even after exposure to liquids with a wide range of pH values (Fig. 5a). Then, we investigated the retention of superomniphobicity of our surfaces at different strain rates. Our contact angle and sliding angle measurements for hexadecane indicated that the hyperelastic superomniphobic surfaces retained their superomniphobicity at both the unstretched and stretched states, even after stretching at strain rates as high as 0.8 s^{-1} (Fig. 5b) and simultaneously stretching and twisting up to 360° (Fig. 5c and Section S5, ESI†). The retention of superomniphobicity is also evident from droplets of hexadecane easily sliding, without any residue, on our hyperelastic surfaces at different degrees of bending and after simultaneous bending and stretching (Section S5, ESI†). Finally, we also investigated the influence of stretch–release cycles on the superomniphobicity of our hyperelastic superomniphobic surfaces at the unstretched and stretched states. First, we subjected our hyperelastic superomniphobic surfaces to multiple abrupt stretch–release cycles (a cycle is manually stretching from the unstretched state to maximum stretch and suddenly releasing back to the unstretched state), and the surfaces retained their superomniphobicity at both the unstretched and stretched states (Movie S4, ESI†). Then, we subjected our hyperelastic superomniphobic surfaces to prolonged stretch–release cycles at a controlled rate (a cycle is stretching from the unstretched state to maximum stretch and then relaxing back to the unstretched state at a displacement rate of 1.6 mm s^{-1} with a tensile tester). Our results indicate that the hyperelastic superomniphobic surfaces retained their superomniphobicity at both the unstretched and stretched states for at least 5000 cycles (Fig. 5d and Movie S5, ESI†). Our hyperelastic superomniphobic surfaces retained their superomniphobicity even after knife scratching (Movie S6, ESI†). Furthermore, we demonstrate that the stress redistribution mechanism is generalizable and is not restrictive to specific mesh geometry, particles and elastomers (Section S6, ESI†). To the best of our knowledge, there are no reports of such hyperelastic superomniphobic surfaces that

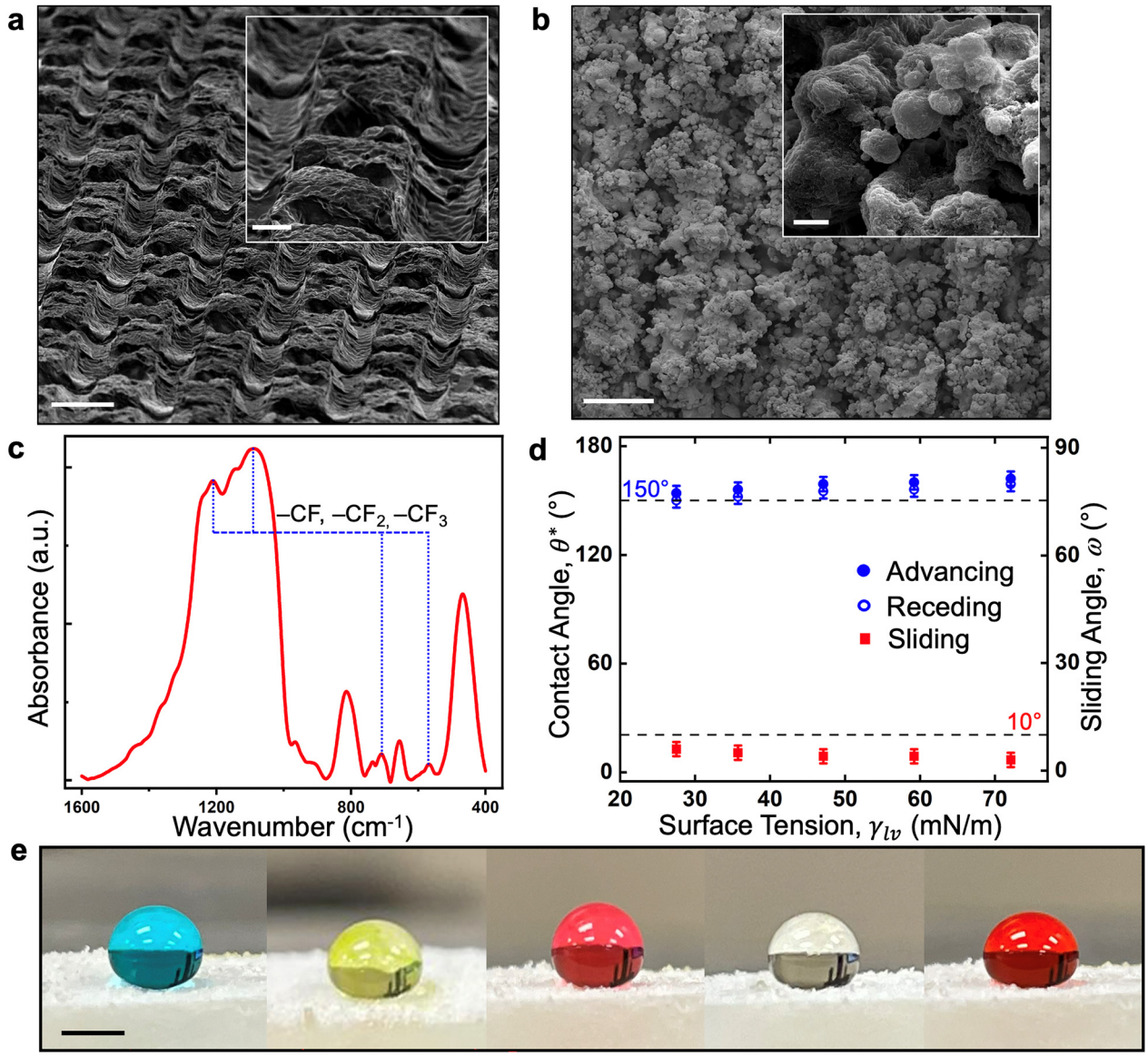

Fig. 3 Hyperelastic superomniphobic surface at the unstretched state. (a) SEM image and inset depicting the morphology of the micromolded siloxane elastomer. (b) SEM image depicting the morphology of the unstretched elastomer with microprotrusions, coated with fluorinated silica nanoparticles. The inset depicts the agglomerates of fluorinated silica nanoparticles. The scale bar in (a) and (b) is 100 μm. The scale bars in insets of (a) and (b) are 30 μm and 5 μm, respectively. (c) FTIR spectrum of the fluorinated silica nanoparticles depicting fluorocarbon peaks. (d) Apparent contact angles and sliding angles for liquids with a wide range of surface tensions on the hyperelastic superomniphobic surface, at the unstretched state. The top dotted line represents a contact angle of 150°, and the bottom dotted line represents a sliding angle of 10°. (e) Droplets of water (blue), glycerol (yellow), ethylene glycol (pink), rapeseed oil (white) and hexadecane (red) beading up on the hyperelastic superomniphobic surface, at the unstretched state. The scale bar is 2 mm.

display sustained superomniphobicity up to 400% strain and 5000 stretch–release cycles.

To better elucidate the underlying wetting physics on our hyperelastic superomniphobic surfaces at different strains, we conducted theoretical analyses. At the unstretched state, the hyperelastic superomniphobic surfaces can be visualized as a hierarchical structure composed of finer particles superimposed on coarser square pillars arranged in a square array (Fig. 1e and 6a). When a liquid droplet comes into contact with such a hierarchical structure at the unstretched state, the Cassie–Baxter equation can be recursively written as

$$\cos\theta^*_{\text{hier\_u}} = f_{\text{sl}}\cos\theta - f_{\text{lv}} \approx \left(\frac{R}{R+D}\right)^2 \cos\bar{\theta}^*_{\text{particle}} - \left[1-\left(\frac{R}{R+D}\right)^2\right] \quad (1)$$

Here $\theta^*_{\text{hier\_u}}$ is the apparent contact angle on the unstretched hyperelastic superomniphobic surface, R is the edge of the

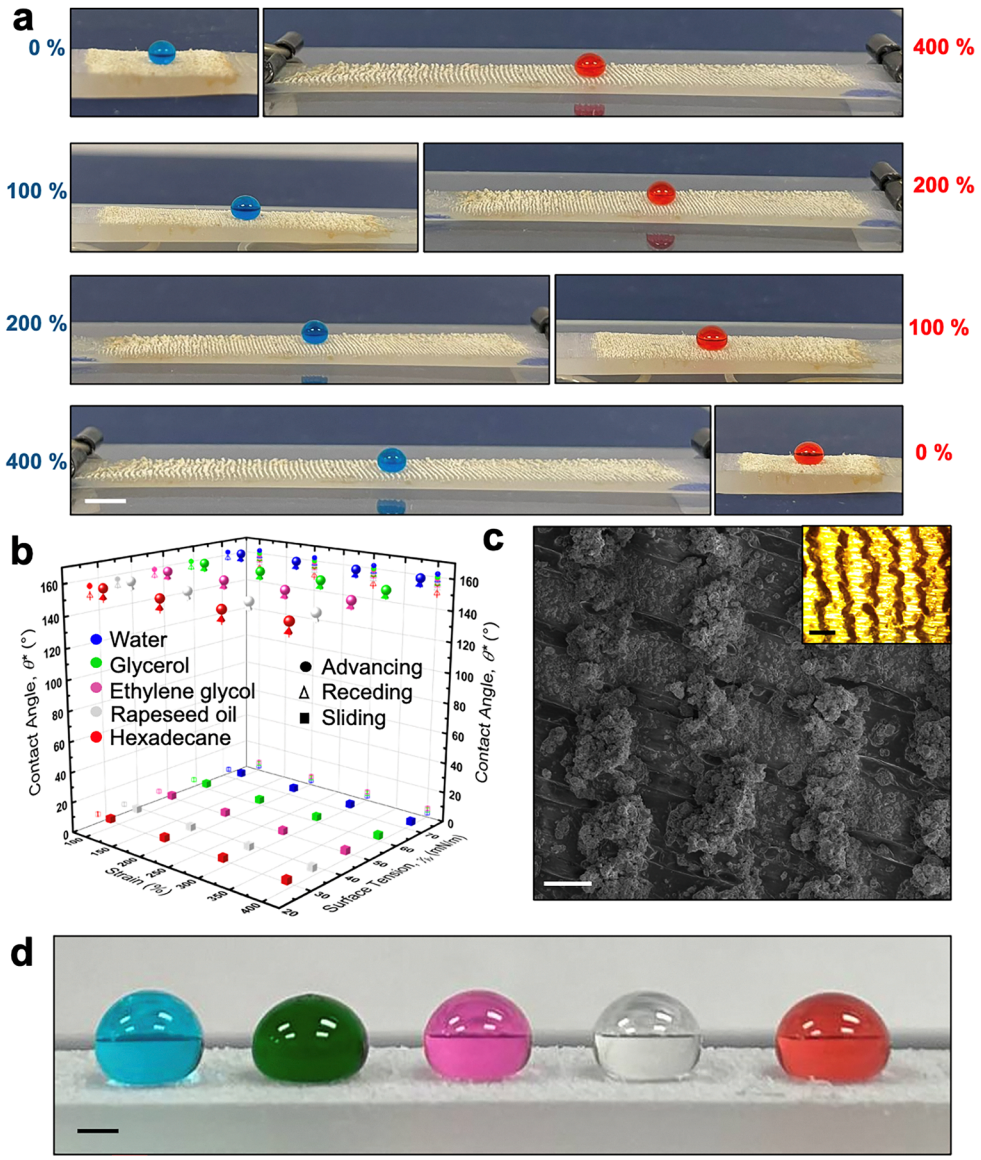

Fig. 4 Hyperelastic superomniphobic surface at the stretched state. (a) Droplets of water (blue) and hexadecane (red) beading up on a hyperelastic superomniphobic surface at 0%, 100%, 200%, 300% and 400% strains. The scale bar is 5 mm. (b) Apparent contact angles and sliding angles for liquids with a wide range of surface tension on the hyperelastic superomniphobic surface, at different strains. (c) SEM image and transmission optical microscopy image (inset) depicting the morphology of the hyperelastic superomniphobic surface at the stretched state. Fluorinated silica nanoparticles are removed due to delamination between the microprotrusions but remain on tops of the microprotrusions (opaque in the inset). The scale bar is 300 μm for the image and 150 μm for the inset. (d) Droplets of water (blue), glycerol (green), ethylene glycol (pink), rapeseed oil (white) and hexadecane (red) beading up on the hyperelastic superomniphobic surface at 400% strain. The scale bar is 1 mm.

pillar, D is the edge-to-edge spacing between the pillars and $\bar{\theta}^*_{\text{particle}}$ is the apparent contact angle on the finer particle texture. Note that $f_{\text{sl}} = \left(\frac{R}{R+D}\right)^2$ is the fraction of solid–liquid interface and $f_{\text{lv}} = 1 - \left(\frac{R}{R+D}\right)^2$ is the fraction of the liquid–air interface at the unstretched state. By measuring $\bar{\theta}^*_{\text{particle}}$ on the finer particle texture (*i.e.*, fluorinated silica particles spray coated on an elastomer without microprotrusions) and the dimensions R and D for the coarser pillar texture, we estimated $\theta^*_{\text{hier\_u}}$ on unstretched hyperelastic superomniphobic surfaces (see Section S7 and Table S1, ESI†). Our results indicate that the experimentally measured contact angles on the hyperelastic superomniphobic surfaces at the unstretched state (*i.e.*, 0% strain) align reasonably well with the theoretical predictions for both water (Fig. 6d) and hexadecane (Fig. 6e). At the uniaxially stretched state, the hyperelastic superomniphobic surfaces can be visualized as a hierarchical structure composed of finer particles superimposed on coarser rectangular pillars arranged in a rectangular array, with an elongated unit cell (Fig. 1f, 6b and c). When a liquid droplet comes into contact with such a hierarchical structure at the stretched state, the Cassie–Baxter equation can be recursively

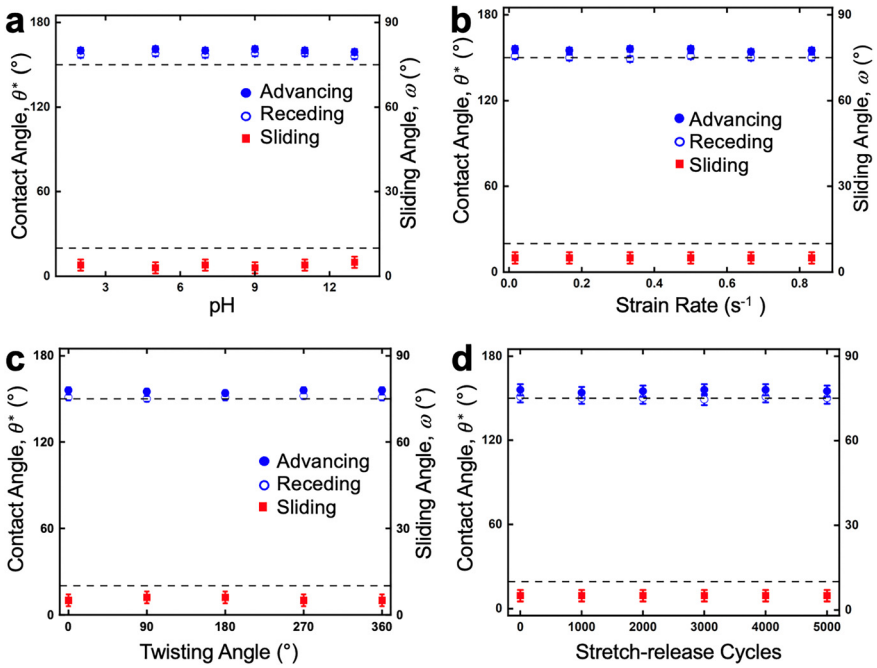

Fig. 5 Flexibility of the hyperelastic superomniphobic surface at the stretched state. (a) Advancing and receding contact angles as well as sliding angles of hexadecane on the hyperelastic superomniphobic surface after exposure to liquids with varying pH. (b) Advancing and receding contact angles as well as sliding angles of hexadecane on the hyperelastic superomniphobic surface after stretching them at different strain rates. (c) Advancing and receding contact angles as well as sliding angles of hexadecane on the hyperelastic superomniphobic surface after simultaneously stretching and twisting at different angles. (d) Advancing and receding contact angles as well as sliding angles of hexadecane on the hyperelastic superomniphobic surface after multiple stretch-release cycles.

written as follows:

$$\cos\theta^*_{\text{hier\_s}} \approx \left(\frac{R_\parallel R_\perp}{(R_\parallel + D_\parallel)(R_\perp + D_\perp)}\right)\cos\bar{\theta}^*_{\text{particle}} - \left(1 - \frac{R_\parallel R_\perp}{(R_\parallel + D_\parallel)(R_\perp + D_\perp)}\right) \quad (2)$$

Here $\theta^*_{\text{hier\_s}}$ is the apparent contact angle on the stretched hyperelastic superomniphobic surface, $R_\parallel$ and $R_\perp$ are the edges of the pillar parallel and perpendicular to the stretching direction, respectively, and $D_\parallel$ and $D_\perp$ are the edge-to-edge spacing between the pillars parallel and perpendicular to the stretching direction, respectively. Note that $f_{\text{sl}} = \frac{R_\parallel R_\perp}{(R_\parallel + D_\parallel)(R_\perp + D_\perp)}$ is the fraction of solid–liquid interface and $f_{\text{lv}} = 1 - \frac{R_\parallel R_\perp}{(R_\parallel + D_\parallel)(R_\perp + D_\perp)}$ is the fraction of liquid–air interface at the stretched state. By measuring $\bar{\theta}^*_{\text{particle}}$ and the dimensions $R_\parallel$, $R_\perp$, $D_\parallel$ and $D_\perp$ for the coarser pillar texture, we estimated $\theta^*_{\text{hier\_s}}$ on the stretched hyperelastic superomniphobic surfaces (see Section S5 and Table S1, ESI†). Our results indicate that the experimentally measured contact angles on the hyperelastic superomniphobic surfaces at the stretched states align reasonably well with the theoretical predictions for both water (Fig. 6d) and hexadecane (Fig. 6e). Furthermore, we estimated the roll of angle ω based on a balance between the work done by gravitational force and the work expended due to adhesion (see Section S8 and Table S2, ESI†).[24] Our results indicate that the experimentally measured sliding angles on the hyperelastic superomniphobic surfaces, at both unstretched and stretched states, align reasonably well with the theoretical predictions (Fig. 6d and e). Finally, we also estimated the breakthrough pressure P_{b} (*i.e.*, the pressure at which the droplet transitions from the Cassie–Baxter state to the Wenzel state) and compared it with the applied pressure $P_{\text{a}} \approx 2\gamma_{\text{lv}}/R_{\text{drop}}$ (here, γ_{lv} and R_{drop} are the liquid surface tension and the droplet radius, respectively) to confirm the wetting state of the droplet on our hyperelastic superomniphobic surfaces, at both unstretched and stretched states. If $P_{\text{b}} > P_{\text{a}}$, the droplet would adopt the Cassie–Baxter state, and if $P_{\text{b}} \leq P_{\text{a}}$, the droplet would transition to the Wenzel state. For a surface composed of an array of pillars, the breakthrough pressure can be determined from a force balance at the liquid–air interface for water and hexadecane (see Section S9, Fig. S4, ESI†). Our results indicate that $P_{\text{b}} > P_{\text{a}}$ for both water (Fig. 6f) and hexadecane (Fig. 6g) on the hyperelastic superomniphobic surfaces, at both unstretched and stretched states studied (see Section S9 and Table S3, ESI†).

3. Conclusions

In summary, we fabricated hyperelastic superomniphobic surfaces using monolithic siloxane elastomers with an array of discrete microprotrusions, coated with fluorinated silica

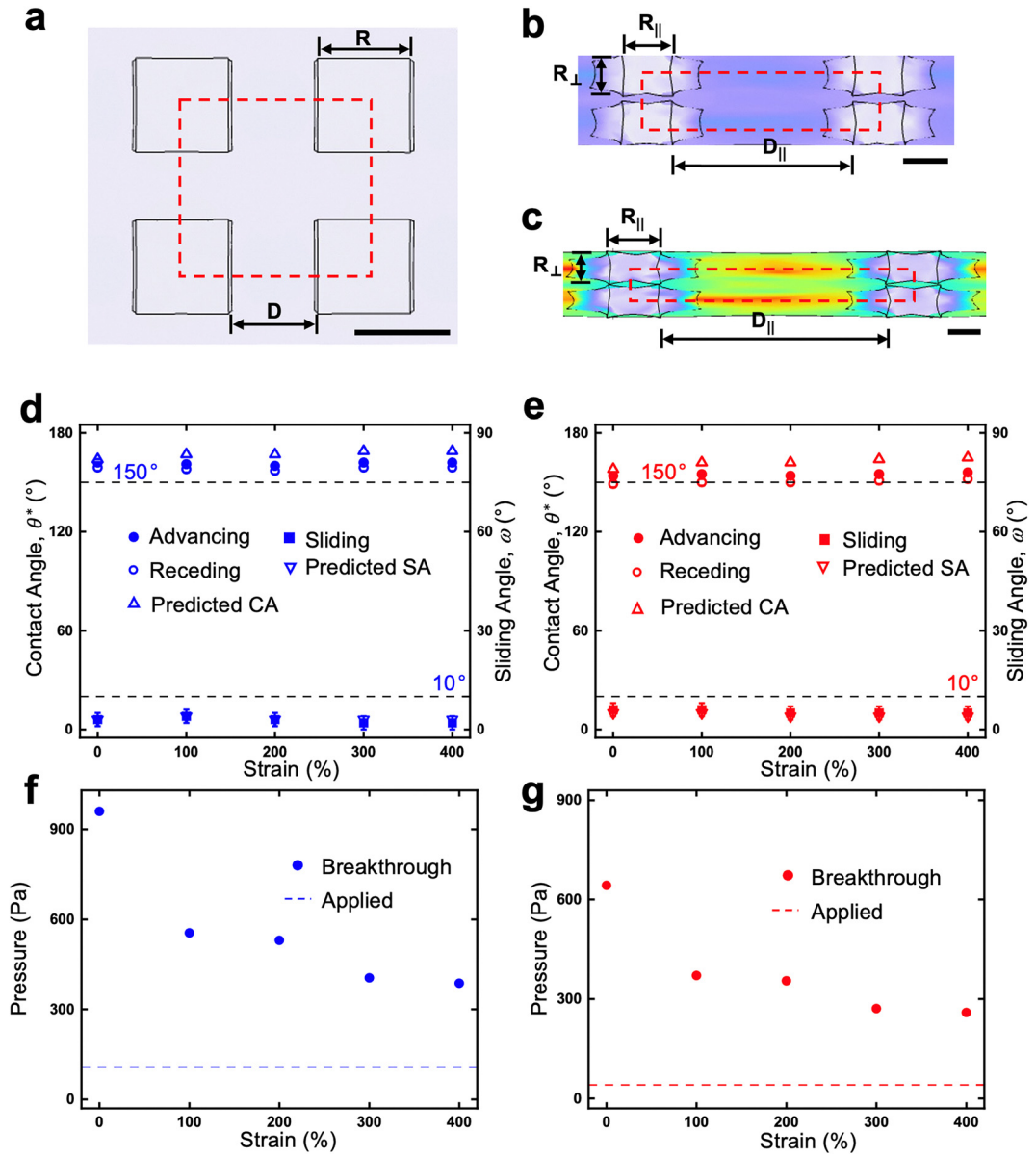

Fig. 6 Estimation of contact angles, sliding angles and breakthrough pressures. Schematics illustrate the unit cell at (a) the unstretched state and (b) 200% and (c) 400% strains. The scale bar is 75 μm. (d) and (e) Contact angles and sliding angles estimated theoretically and measured experimentally for water and hexadecane, respectively, on hyperelastic superomniphobic surfaces at different strains. The top dotted line represents a contact angle of 150°, and the bottom dotted line represents a sliding angle of 10°. (f) and (g) Breakthrough pressures and applied pressures estimated theoretically for water and hexadecane, respectively, on hyperelastic superomniphobic surfaces at different strains.

nanoparticles. The combination of re-entrant texture and low solid surface energy of the fluorinated silica nanoparticles resulted in superomniphobicity. During elongation, the microprotrusions on the hyperelastic material redistributed the stresses out-of-plane, leaving the tops of the microprotrusions nearly stress-free, thereby reducing delamination of the fluorinated silica nanoparticle coating. As a result, the hyperelastic superomniphobic surfaces displayed superomniphobicity at both the unstretched and the stretched states, even at 400% strain and after 5000 stretch–release cycles. Furthermore, through systematic experiments and theoretical analyses, we studied the influence of elongation on contact angles, sliding angles and breakthrough pressures on our hyperelastic superomniphobic surfaces. While our hyperelastic superomniphobic surfaces can retain both stretchability and superomniphobicity against liquids (Section S10, ESI†) as well as against abrasion due to touch and blade scratch tests, further efforts are required to improve their durability against severe solid abrasion. We envision that our engineered hyperelastic superomniphobic surfaces will have a wide range of applications in wearable electronics, textiles, artificial skins, droplet manipulation and protective wraps.

4. Experimental

4.1 Fabrication of hyperelastic superomniphobic surfaces

Hyperelastic surfaces with microprotrusions were fabricated using an Ecoflex 00-50 (Smooth-on) elastomer *via* micromolding with 304 stainless-steel mesh (McMaster-Carr), which has an opening size ≈75 μm and a wire diameter ≈55 μm. The elastomer was cured at room temperature for 24 hours. The surface of the elastomer with microprotrusions was then brush coated with a layer (∼20 μL cm^{-2}) of polyurethane-based adhesive (VytaFlex 00-10, smooth-on), followed by spray coating at an air pressure ≈10 psi and a distance ≈15 cm with a fluorinated silica nanoparticle suspension.

4.2 Fabrication of fluorinated silica nanoparticle suspension

10 mg ml^{-1} of fumed silica nanoparticles (7 nm, Sigma-Aldrich) was dispersed in hexane *via* ultrasonication. 0.3 mL of heptadecafluoro-1,1,2,2-tetrahydrodecyl trichlorosilane (Gelest) was then added to the particle suspension and mixed using a vortexer (Fisher) at room temperature for three days.

4.3 Contact angle and sliding angle measurements

The contact angles and sliding angles of liquid droplets on the fabricated surfaces were measured using a contact angle goniometer (Ramé-Hart 260). The advancing contact angle and receding contact angle were measured by increasing and decreasing, respectively, the volume of a droplet on the surface using a micrometer syringe (Gilmont). The sliding angles were measured by slowly tilting the surface until the droplet (∼10 μL) started sliding on the surface. At least six measurements were performed on each surface at spatially distinct locations.

4.4 Morphology characterization

The surface morphology was characterized using a scanning electron microscope (SEM; Thermo Fisher Phenom Pharos) at 5 kV. The samples were sputter coated with a thin film of gold prior to imaging (Cressington 108).

4.5 FTIR characterization

Samples for FTIR (Thermo Scientific Nicolet iS50) were prepared by mixing the desired material with KBr powder to form a pellet. Samples were analyzed with a DTGS/KBr detector, and spectra were recorded at a 2 cm^{-1} resolution with 32 scans. Background spectra were obtained with an empty pellet holder.

4.6 Characterization of mechanical properties

The quasi-static mechanical properties were measured using ASTM type I specimens in a tensile tester (Instron).[39,40] Force was measured with a 2 kN load cell (Instron), and displacement was measured using the crosshead velocity (20 mm min^{-1}). Specimen dimensions were used to convert the force–displacement curves to stress–strain curves.

4.7 Numerical simulations

The 3D geometric models of the Ecoflex 00-50 elastomers (0.87 mm length × 0.27 mm width × 1 mm height) without and with microprotrusions (75 μm length × 75 μm width × 40 μm height, similar to the experimental samples) were built using COMSOL®. The nonlinear structural materials module in COMSOL® was used for analysis. A mesh refinement study was conducted to determine the accuracy and convergence of the mesh. The elastomer was modeled using a hyperelastic isotropic Yeoh model[41–43] by calculating the energy density $U = \sum_{i=1}^{N} C_{i0}(\bar{I}_1 - 3)^i + \sum_{i=1}^{N} \frac{1}{D_i}(J-1)^{2i}$. Here $\bar{I}_1 = \mathrm{tr}[\mathrm{dev}(\mathbf{FF})^{\mathrm{T}}]$, J = $\det(\mathbf{F})$, **F** is the deformation gradient, and C_{i0} and D_i are the material parameters. In the model, $N = 3$, $C_{10} = 0.019$, $C_{20} = 0.0009$, $C_{30} = -4.75 \times 10^{-6}$ MPa, and $D_1 = D_2 = D_3 = 0$.[44] Equal prescribed displacements ($d = \pm 1.6$ mm) were applied in opposite directions along the length of the elastomers to simulate the stretching process. A mesh-independence check was performed to confirm that the numerical results were virtually insensitive to further mesh refinement.

Author contributions

M. J. Zarei: methodology, investigation, analysis, and writing – original draft. S. Pillai: methodology, investigation, analysis, and writing – original draft. O. Eldaly: methodology, investigation, analysis, and writing – original draft. A. M. Rather: methodology, investigation, and analysis. S. Vallabhuneni: methodology. M. A. Zikry: investigation, supervision, and writing – original draft. A. K. Kota: conceptualization, investigation, supervision, and writing – original draft.

Conflicts of interest

There are no conflicts to declare.

Data availability

The data supporting this article have been included as part of the ESI.†

Acknowledgements

A. K. K. acknowledges support from the National Science Foundation under grant 2245427, National Institutes of Health grants R21EB033960 and R01HL166724, and Congressionally Directed Medical Research Programs grant HT94252310663.

References

1 T. L. Liu and C. J. C. Kim, Turning a surface superrepellent even to completely wetting liquids, *Science*, 2014, **346**, 1096–1100.
2 B. Su, Y. Tian and L. Jiang, Bioinspired interfaces with superwettability: from materials to chemistry, *J. Am. Chem. Soc.*, 2016, **138**, 1727–1748.
3 H. Zhou, Y. Zhao, H. Wang and T. Lin, Recent Development in Durable Super-Liquid-Repellent Fabrics, *Adv. Mater. Interfaces*, 2016, **3**, 1600402.

4 J. Liu, L. Ye, Y. Sun, M. Hu, F. Chen, S. Wegner, V. Mailänder, W. Steffen, M. Kappl and H. J. Butt, Elastic superhydrophobic and photocatalytic active films used as blood repellent dressing, *Adv. Mater.*, 2020, **32**, 1908008.
5 J. N. Wang, Y. Q. Liu, Y. L. Zhang, J. Feng, H. Wang, Y. H. Yu and H. B. Sun, Wearable superhydrophobic elastomer skin with switchable wettability, *Adv. Funct. Mater.*, 2018, **28**, 1800625.
6 H. Jinno, K. Fukuda, X. Xu, S. Park, Y. Suzuki, M. Koizumi, T. Yokota, I. Osaka, K. Takimiya and T. Someya, Stretchable and waterproof elastomer-coated organic photovoltaics for washable electronic textile applications, *Nat. Energy*, 2017, **2**, 780–785.
7 D. Wang, Q. Sun, M. J. Hokkanen, C. Zhang, F. Y. Lin, Q. Liu, S. P. Zhu, T. Zhou, Q. Chang and B. He, Design of robust superhydrophobic surfaces, *Nature*, 2020, **582**, 55–59.
8 W. Wang, H. Vahabi, S. Movafaghi and A. K. Kota, Superomniphobic Surfaces with Improved Mechanical Durability: Synergy of Hierarchical Texture and Mechanical Interlocking, *Adv. Mater. Interfaces*, 2019, **6**, 1900538.
9 J. Verma, G. J. Bennett and S. Goel, Design considerations to fabricate multifunctional superomniphobic surfaces: A review, *Vacuum*, 2023, **209**, 111758.
10 J. Ju, X. Yao, X. Hou, Q. Liu, Y. S. Zhang and A. Khademhosseini, A highly stretchable and robust non-fluorinated superhydrophobic surface, *J. Mater. Chem. A*, 2017, **5**, 16273–16280.
11 X. Hu, C. Tang, Z. He, H. Shao, K. Xu, J. Mei and W. M. Lau, Highly stretchable superhydrophobic composite coating based on self-adaptive deformation of hierarchical structures, *Small*, 2017, **13**, 1602353.
12 S. Wang, X. Yu and Y. Zhang, Large-scale fabrication of translucent, stretchable and durable superhydrophobic composite films, *J. Mater. Chem. A*, 2017, **5**, 23489–23496.
13 X. Zhou, J. Liu, W. Liu, W. Steffen and H. J. Butt, Fabrication of Stretchable superamphiphobic surfaces with deformation-induced rearrangeable structures, *Adv. Mater.*, 2022, **34**, 2107901.
14 S. Tian, X. Wang, W. Qin, S. Yin, T. Tan, Y. Tian and C. Wang, Ultra-robust, stretchable electrodes based on superamphiphobic surface for personal exercise monitoring, *Chem. Eng. J.*, 2023, **452**, 139421.
15 A. K. Kota, W. Choi and A. Tuteja, Superomniphobic surfaces: Design and durability, *MRS Bull.*, 2013, **38**, 383–390.
16 T. Young, III, An essay on the cohesion of fluids, *Philos. Trans. R. Soc. London*, 1805, **95**, 65–87.
17 Z. Chu and S. Seeger, Superamphiphobic surfaces, *Chem. Soc. Rev.*, 2014, **43**, 2784–2798.
18 H. Vahabi, W. Wang, S. Movafaghi and A. K. Kota, Free-standing, flexible, superomniphobic films, *ACS Appl. Mater. Interfaces*, 2016, **8**, 21962–21967.
19 A. Tuteja, W. Choi, M. Ma, J. M. Mabry, S. A. Mazzella, G. C. Rutledge, G. H. McKinley and R. E. Cohen, Designing superoleophobic surfaces, *Science*, 2007, **318**, 1618–1622.
20 A. Lafuma and D. Quéré, Superhydrophobic states, *Nat. Mater.*, 2003, **2**, 457–460.
21 S. Vallabhuneni, S. Movafaghi, W. Wang and A. K. Kota, Superhydrophobic coatings for improved performance of electrical insulators, *Macromol. Mater. Eng.*, 2018, **303**, 1800313.
22 R. N. Wenzel, Resistance of solid surfaces to wetting by water, *Ind. Eng. Chem.*, 1936, **28**, 988–994.
23 A. Cassie and S. Baxter, Wettability of porous surfaces, *Trans. Faraday Soc.*, 1944, **40**, 546–551.
24 R. E. Johnson Jr and R. H. Dettre, Contact angle hysteresis. III. Study of an idealized heterogeneous surface, *J. Phys. Chem.*, 1964, **68**, 1744–1750.
25 M. Nosonovsky and B. Bhushan, Superhydrophobic surfaces and emerging applications: Non-adhesion, energy, green engineering, *Curr. Opin. Colloid Interface Sci.*, 2009, **14**, 270–280.
26 H. Vahabi, W. Wang, K. C. Popat, G. Kwon, T. B. Holland and A. K. Kota, Metallic superhydrophobic surfaces via thermal sensitization, *Appl. Phys. Lett.*, 2017, **110**, 25.
27 A. Marmur, Wetting on hydrophobic rough surfaces: to be heterogeneous or not to be?, *Langmuir*, 2003, **19**, 8343–8348.
28 C. Furmidge, Studies at phase interfaces. I. The sliding of liquid drops on solid surfaces and a theory for spray retention, *J. Colloid Sci.*, 1962, **17**, 309–324.
29 W. Wang, J. Sun, S. Vallabhuneni, B. Pawlowski, H. Vahabi, K. Nellenbach, A. C. Brown, F. Scholle, J. Zhao and A. K. Kota, On-demand, remote and lossless manipulation of biofluid droplets, *Mater. Horiz.*, 2022, **9**, 2863–2871.
30 A. K. Kota, G. Kwon and A. Tuteja, The design and applications of superomniphobic surfaces, *NPG Asia Mater.*, 2014, **6**, e109.
31 W. Wang, H. Vahabi, S. Movafaghi and A. K. Kota, Superomniphobic surfaces with improved mechanical durability: Synergy of hierarchical texture and mechanical interlocking, *Adv. Mater. Interfaces*, 2019, **6**, 1900538.
32 G. T. Yun, W. B. Jung, M. S. Oh, G. M. Jang, J. Baek, N. I. Kim, S. G. Im and H. T. Jung, Springtail-inspired superomniphobic surface with extreme pressure resistance, *Sci. Adv.*, 2018, **4**, eaat4978.
33 S. Movafaghi, M. D. Cackovic, W. Wang, H. Vahabi, A. Pendurthi, C. S. Henry and A. K. Kota, Superomniphobic Papers for On-Paper pH Sensors, *Adv. Mater. Interfaces*, 2019, **6**, 1900232.
34 W. Wang, J. Salazar, H. Vahabi, A. Joshi-Imre, W. E. Voit and A. K. Kota, Metamorphic superomniphobic surfaces, *Adv. Mater.*, 2017, **29**, 1700295.
35 S. Movafaghi, W. Wang, A. Metzger, D. D. Williams, J. D. Williams and A. K. Kota, Tunable superomniphobic surfaces for sorting droplets by surface tension, *Lab Chip*, 2016, **16**, 3204–3209.
36 R. Campos, A. J. Guenthner, A. J. Meuler, A. Tuteja, R. E. Cohen, G. H. McKinley, T. S. Haddad and J. M. Mabry, Superoleophobic Surfaces through Control of Sprayed-on Stochastic Topography, *Langmuir*, 2012, **28**, 9834–9841.
37 R. Molina, J. M. Teixidó, C. W. Kan and P. Jovančić, Hydrophobic coatings on cotton obtained by in situ plasma polymerization of a fluorinated monomer in ethanol solutions, *ACS Appl. Mater. Interfaces*, 2017, **9**, 5513–5521.

38 J. D. Brassard, D. K. Sarkar and J. Perron, Synthesis of monodisperse fluorinated silica nanoparticles and their superhydrophobic thin films, *ACS Appl. Mater. Interfaces*, 2011, **3**, 3583–3588.
39 A. L. Gershon, D. P. Cole, A. K. Kota and H. A. Bruck, Nanomechanical characterization of dispersion and its effects in nano-enhanced polymers and polymer composites, *J. Mater. Sci.*, 2010, **45**, 6353–6364.
40 A. L. Gershon, A. K. Kota and H. A. Bruck, Characterization of quasi-static mechanical properties of polymer nanocomposites using a new combinatorial approach, *J. Compos. Mater.*, 2009, **43**, 2587–2598.
41 Y. Chi, Y. Hong, Y. Zhao, Y. Li and J. Yin, Snapping for high-speed and high-efficient butterfly stroke–like soft swimmer, *Sci. Adv.*, 2022, **8**, eadd3788.
42 O. H. Yeoh, Some forms of the strain energy function for rubber, *Rubber Chem. Technol.*, 1993, **66**, 754–771.
43 J. S. Bergstrom, *Mechanics of solid polymers: theory and computational modeling*, William Andrew, NY, 2015.
44 Y. Chi, Y. Tang, H. Liu and J. Yin, Leveraging Monostable and Bistable Pre-Curved Bilayer Actuators for High-Performance Multitask Soft Robots, *Adv. Mater. Technol.*, 2020, **5**, 2000370.